

See discussions, stats, and author profiles for this publication at: <https://www.researchgate.net/publication/6951917>

# Universal and State-Resolved Imaging of Chemical Dynamics

ARTICLE *in* THE JOURNAL OF PHYSICAL CHEMISTRY A · NOVEMBER 2005

Impact Factor: 2.69 · DOI: 10.1021/jp0526086 · Source: PubMed

---

CITATIONS

32

---

READS

18

5 AUTHORS, INCLUDING:



Suk Kyoung Lee

Wayne State University

23 PUBLICATIONS 450 CITATIONS

SEE PROFILE

## FEATURE ARTICLE

### Universal and State-Resolved Imaging of Chemical Dynamics

Dave Townsend, Wen Li, Suk Kyoung Lee, Richard L. Gross, and Arthur G. Suits\*

*Department of Chemistry, Wayne State University, Detroit, Michigan 48202, Chemistry Department, Brookhaven National Laboratory, Upton, New York 11973, and Department of Chemistry, Stony Brook University, Stony Brook, New York 11794*

*Received: May 18, 2005; In Final Form: July 18, 2005*

We showcase the use of high-resolution ion imaging with complementary state-resolved and “universal” vacuum ultraviolet probes to address a broad range of fundamental problems in chemical reaction dynamics. Examples from our recent work include applications in state-correlated unimolecular reactions, ion pair dissociation dynamics and spectroscopy, crossed-beam reactive scattering, and atomic angular momentum polarization in photodissociation. These studies are all directed to achieving a detailed understanding of atomic and molecular interactions, with particular emphasis on reaction mechanisms outside the scope of transition state theory; on spectroscopy and dynamics of highly excited, transient species; on nonadiabatic reaction mechanisms; and on chemical dynamics in polyatomic systems.

#### I. Introduction

The evolution of chemical understanding has proceeded, on one hand, through the use of simple conceptual models developed without regard to fundamental theoretical underpinnings, and on the other hand through rigorous application of quantum and statistical mechanics to chemical problems. Chemical dynamics<sup>1</sup> is the field where these two descriptions meet and must be reconciled. It is concerned both with identifying the appropriate theoretical framework in which to place the relevant physical laws and in pursuing the detailed experimental studies that are essential to validate the theoretical models and justify the approximations on which they rest. However, even if we are given a satisfactory theoretical framework, the overwhelming complexity of practical chemical systems means that complete first-principles modeling is not a viable proposition. Instead, we require insight into the underlying principles and guiding trends if we are to develop useful and accurate predictive models for real chemical systems. The development of this insight is among the central goals of chemical dynamics investigations.

Experimental studies in chemical reaction dynamics have blossomed in recent years with extraordinary progress on many

fronts. Sophisticated experimental and theoretical techniques have brought to light the intimate details of molecular interactions: reactive encounters are probed under single collision conditions,<sup>2</sup> with quantum state specificity,<sup>3,4</sup> and sometimes with full rotational resolution<sup>5,6</sup> and product quantum state correlations;<sup>7,8</sup> reactions are studied in the “real time” of a single vibrational period;<sup>9</sup> the properties of the transition state itself have been revealed directly in experiments.<sup>10</sup> Our current challenge lies in adapting these powerful techniques to address important chemical problems at the limit of our reach: reaction dynamics involving multiple potential energy surfaces and nonadiabatic processes; the properties and reactive behavior of radicals, superexcited molecules and other transient species; and the detailed reaction dynamics of polyatomic molecules. Selected examples of our recent work addressing these issues are presented in the pages that follow.

Our effort exploits recent advances in ion and electron imaging techniques,<sup>11–14</sup> in molecular beam scattering,<sup>15–17</sup> and in development of new extreme ultraviolet light sources<sup>18</sup> and new spectroscopic approaches,<sup>19,20</sup> to extend the range of chemical dynamics studies. Our particular experimental emphasis is on combining high-resolution state-resolved imaging studies with universal vacuum ultraviolet (VUV) probes. The

\* Corresponding author. E-mail: asuits@chem.wayne.edu.

Dave Townsend was born in 1974 in Rugby, England. He obtained a B.Sc. in Chemistry at The University of Nottingham, where he remained for his Ph.D. studies in the research group of Katharine Reid. After spending time as a postdoc in Oxford working with Tim Softley, he then moved to Stony Brook to join the Suits group in 2001. Dave is currently a Visiting Fellow at the Canadian National Research Council in Ottawa, working in the area of coherent quantum control of molecular processes using femtosecond laser pulses.

Wen Li was born in 1977 in Zhejiang, China. He studied chemistry and physics in Beijing University and graduated with a B.S. and honors in 2000. He joined the Suits group as a graduate student studying photodissociation and photoionization dynamics using the velocity map imaging technique. Currently his research focuses on reactive scattering of radicals and molecules utilizing state-resolved REMPI probes and crossed beam imaging.

Suk Kyoung Lee was born in 1973 in Seoul, Korea. She received her B.A. and M.A. in chemistry from Ewha Woman's University in Korea. She began graduate studies at SUNY at Stony Brook University in the Suits group in 2001. Her current research interests focus on the orbital polarization of atomic photofragments in photodissociation using the DC slice imaging technique.

Richard Gross received his B.S. in Physics and Chemistry from SUNY at Stony Brook, where he is currently pursuing graduate studies in the group of Professor Arthur Suits. His research focuses on the reactive scattering of simple chain and branched alkanes with atomic oxygen and chlorine via velocity map imaging.

Arthur G. Suits obtained a B.S. in chemistry from the University of Missouri, Columbia, in 1986, and a Ph.D. in 1991 from the University of California, Berkeley, under the direction of Yuan T. Lee. He did postdoctoral work with Paul Houston at Cornell University 1991–1993 and then returned to Lawrence Berkeley National Laboratory to direct the Chemical Dynamics Beamline at the Advanced Light Source from 1993 to 2000. In 2000 he joined the faculty of Stony Brook University with a joint appointment at Brookhaven National Laboratory. In 2004 he moved to Wayne State University as Professor of Chemistry.

present article represents a snapshot of our work over the past three years and encompasses experiments at Stony Brook University, Brookhaven National Laboratory, and now Wayne State University. This work is strongly coupled to theory, and indeed the strong interaction with theory is one of the hallmarks of chemical dynamics investigations. Nevertheless, there are also immediate practical implications of these studies in diverse areas such as combustion, atmospheric and interstellar chemistry, and these will be featured when they arise in the pages that follow.

The remainder of this article is organized into distinct sections covering a range of experimental investigations into the areas outlined above. Section II introduces the ion imaging technique and highlights recent experimental advances from our laboratory and others. Section III illustrates application of high-resolution ion imaging to measurements of correlated state distributions in the molecular products of formaldehyde decomposition. These results reveal the importance of a reaction mechanism that avoids the conventional reaction path, challenging conventional transition state theory. An example of application of VUV photodissociation to *ion pair* products is presented in section IV. The reaction dynamics of ground state and electronically excited oxygen atoms with alkanes are contrasted in a set of crossed-beam imaging experiments presented in section V. Section VI introduces the use of imaging to investigate atomic orbital polarization in the photodissociation of ozone. This is an example of a vector correlation study, an area in which many of the virtues of ion imaging are brought to the fore. Finally, section VII presents a brief summary and outlook for the future of chemical dynamics and ion imaging methods.

## II. Experimental Approach: DC Slice Imaging with Megapixel Resolution

The ion-imaging technique, as first introduced by Chandler and Houston,<sup>11</sup> and the high-resolution, velocity mapping variant developed by Eppink and Parker<sup>12</sup> have become widely used in studies of molecular photodissociation and reactive scattering.<sup>21,22</sup> By projecting the entire three-dimensional (3D) distribution of recoiling atomic or molecular fragments onto a two-dimensional (2D) position sensitive microchannel plate (MCP) detector coupled to a CCD camera, the complete velocity and angular distributions for a given process may be extracted from a single image. A compelling feature of this approach is that the result is evident at a glance, at least qualitatively. Quantitative analysis of the image then yields rich detail: here, a picture is worth upward of  $10^6$  “words”, as we shall show. In conventional ion imaging, however, to recover the final product velocity distributions, one must employ some form of tomographic transformation to reconstruct the 3D distribution of recoiling fragments from the 2D projection. This is illustrated schematically in Figure 1. The inverse Abel transform is the most commonly cited method for performing this task, although a number of alternative approaches have been developed in recent years; the reader is directed to ref 23 for a detailed review.

There are several shortcomings associated with the projection-reconstruction approach. These include noise and artifacts sometimes associated with the inversion, compromised velocity resolution, and the requirement that the recoiling fragment distribution (or, more specifically, the distribution of *fragments*) is cylindrically symmetric about an axis parallel to the plane of the imaging detector (see Figure 1A). Alternative approaches have long been sought to circumvent these problems and to measure the quantity of interest – the velocity distribution – directly. One such strategy has been the development of data analysis techniques to extract the full velocity and angular information directly from the raw 2D projection images,<sup>24–26</sup> and forward convolution methods of this type have enjoyed a considerable degree of success.<sup>17,27–31</sup> More recently, efforts to stretch the ion cloud along the flight direction then slice the central section of the fragment distribution have proven very successful, and these have displaced virtually all other approaches in our own laboratory. This idea can be traced to early efforts by Tonokura and Suzuki<sup>32</sup> using “laser sheet” ionization, and more recently efforts by Kitsopoulos and co-workers.<sup>33</sup> In the latter approach, the cloud of ionic fragments is allowed to expand under field free conditions for a short time prior to the application of a pulsed electric field that then accelerates them out of the interaction region. This serves to stretch the spread in arrival time,  $\Delta t$ , of the fragments at the 2D position sensitive detector to on the order of several hundred nanoseconds so that application of a narrow (and experimentally feasible) timing gate at the detector is then sufficient to sample only the central section of the product distribution. One disadvantage with this approach, however, is that to create a field free expansion region for the recoiling ions, a fine mesh grid must be introduced into the ion optics assembly; this compromises the velocity mapping characteristics of the experimental setup and leads to a loss of resolution in the sliced image.

We recently developed an alternative approach, termed direct current (DC) slice imaging, to preserve the advantages of velocity focusing while at the same time directly measuring the velocity distribution.<sup>34</sup> This technique is similar in spirit to that described by Kitsopoulos et al., but no grids are employed and no focusing elements are pulsed. A more comprehensive discussion may be found in refs 34 and 14.

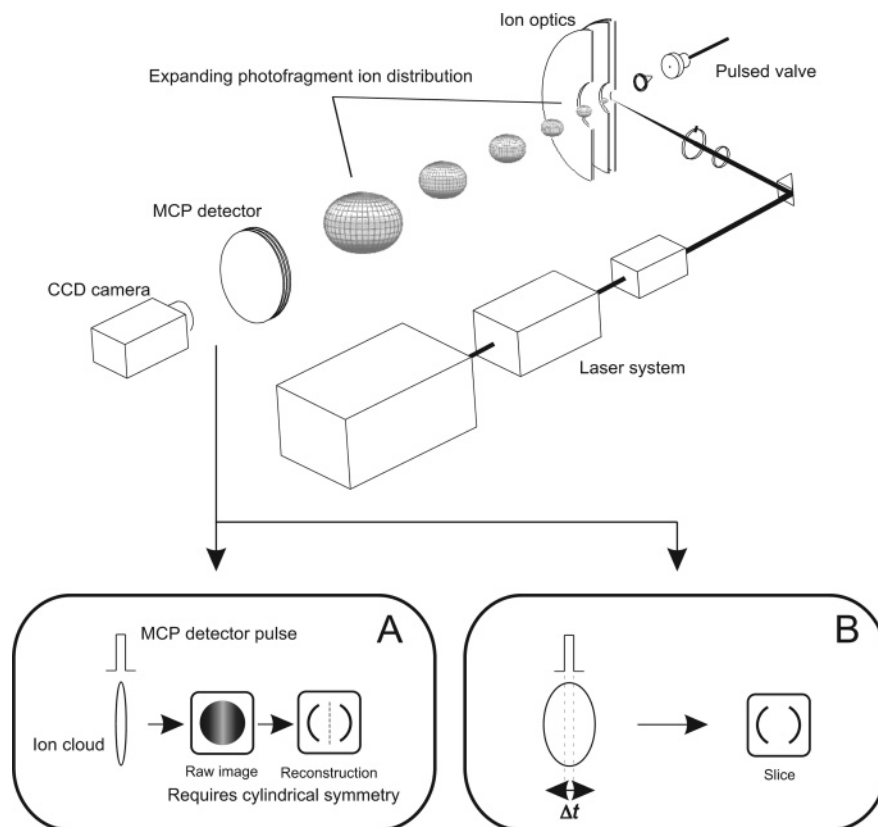


**Figure 1.** Schematic illustration of the ion-imaging setup. (A) In a conventional velocity mapping arrangement, the spread in the arrival time of the fragment ions at the detector is small. The entire distribution is sampled and the central section must therefore be reconstructed. (B) The goal of slice imaging methods is to elongate the ion cloud as it travels from the laser interaction region to the detector, enabling the central section to be sampled directly.

The main advantage of the velocity mapping scheme over previous imaging approaches, as described in detail in the well-known work of Eppink and Parker,<sup>12</sup> is that image blurring due to any spatial spread in the ionization volume is greatly reduced. This is achieved using a simple ion lens assembly, as shown schematically in Figure 2A. The critical parameter for achieving good velocity focusing (i.e., the mapping of fragment ions of a given velocity onto the same point on the detector, irrespective of where they were formed in the ionization volume) is the ratio of the voltages applied to the individual lens elements. Under these “traditional” velocity mapping conditions, the expanding ion cloud is projected onto the detector with a temporal spread in arrival time of  $\Delta t \sim 30$  ns or less. This is illustrated in simulated trajectory calculations of  $^{16}\text{O}^+$  ions produced with 0.5 eV kinetic energy and accelerated with a repeller voltage of  $V_R = +2500$  V, as presented in Figure 2A.

By reducing  $V_R$  to +500 V (and scaling the voltage on  $L_1$  accordingly), as shown in Figure 2B, one is able to increase  $\Delta t$ , to a little over 100 ns. This is a simple consequence of the reduced electric field in the interaction region, leading to a longer “turn-around” time for photofragments that are initially scattered away from the detector; almost all of the ion cloud elongation therefore occurs in this initial region. Further significant reductions in  $V_R$  become somewhat impractical owing to the finite size of the detector and decreased kinetic energy of the ions impacting at the detector leading to poor signal gain. These problems may be easily overcome, however, by the simple insertion of additional lenses into the ion optics assembly, as can be seen from the trajectory simulation in Figure 2C. The inclusion of just one new lens,  $L_2$ , enables the field in the interaction region (i.e., the region between  $L_G$  and  $L_1$ ) to be reduced considerably (for a given value of  $V_R$ ) relative to the

case shown in Figure 2B. The voltage applied to  $L_2$  is then tailored to restore good velocity focusing conditions and the experimental resolution of the instrument is preserved. The spread in ion arrival time is again increased considerably ( $\Delta t$  of 230 ns) although the image size at the detector and ion impact energy are maintained. In fact, the additional lens results in a further improvement in velocity focusing, limited to 2% or so in the standard velocity mapping configuration but better than 0.2% in the three lens system. Application of a narrow gate of  $\leq 40$  ns to the MCP assembly is then sufficient to implement the slicing approach experimentally for this particular test case. As noted previously, however, the “turn around” time of the ions in the interaction region is responsible for the stretching effect we observe, and this will inherently lead to a greater degree of elongation (and therefore better slicing) for fast and/or heavy ion fragments, as illustrated for the case of  $^{35}\text{Cl}^+$  ions in a previous publication.<sup>13</sup> In fact, the stretching time is simply given by  $\Delta t = 2p/qE$ , where  $p$  is the ion momentum along the flight direction,  $E$  is the electric field in the interaction region, and  $q$  is the ion charge.<sup>14</sup> This implies that both fragments in a photodissociation event will exhibit the same ion cloud stretching because they will necessarily have the same linear momentum.

Extensive simulations and experiments carried out in our group demonstrate that the incorporation of a second additional ion lens,  $L_3$  enables the field in the interaction region to be reduced still further, while further improving velocity focusing conditions, with  $\Delta t$  increased to around 400 ns for the example system (see Figure 2D). In our view, this “three lens” scheme represents an optimal compromise for most applications, achieving exceptional velocity focusing and slicing while preserving experimental simplicity. It should be noted that in



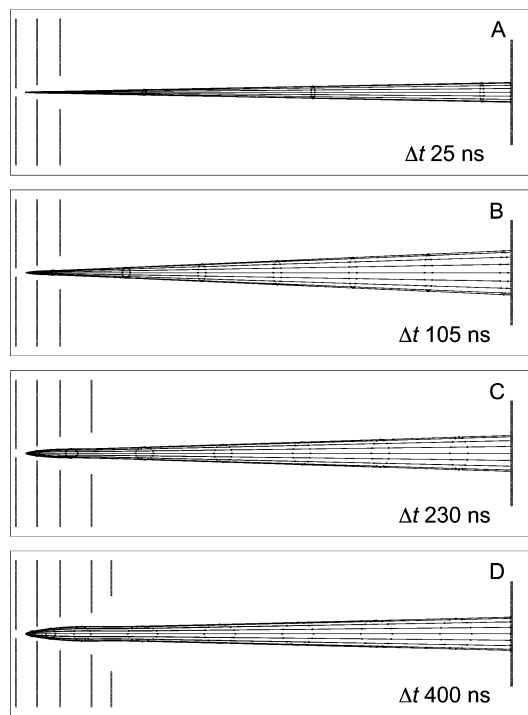


**Figure 2.** Simulations showing the expansion of the photofragment ion cloud (in 1.5  $\mu$ s intervals) for  $^{16}\text{O}^+$  ions with 0.5 eV kinetic energy. In each figure the leftmost electrode is the repeller ( $V_R$ ) and the rightmost electrode is grounded ( $L_G$ ). Potential settings: (A) one lens,  $V_R + 2500$  V,  $L_1 + 1775$  V; (B) one lens,  $V_R + 500$  V,  $L_1 + 355$  V; (C) two lenses,  $V_R + 500$  V,  $L_1 + 430$  V,  $L_2 + 384$  V; (D) three lenses,  $V_R + 500$  V,  $L_1 + 460$  V,  $L_2 + 430$  V,  $L_3 + 342$  V. Each ion lens element is 2 mm thick. In (D) lens aperture diameters are 8, 12, 30, 40, and 70 mm. Lens spacing is 18, 20, 30, and 18 mm from left to right.

parallel to our own development of this method, a very similar “3-D imaging” approach employing multiple ion lens elements was also demonstrated by Lin et al.<sup>35</sup>

As a demonstration of the DC slice imaging principle we show photodissociation of  $\text{NO}_2$  at 355 nm (Figure 3). In this example, the recoil energy in the  $\text{O}(^3\text{P})$  atomic fragment reflects the internal energy that is partitioned into the NO cofragment. The two major peaks indicate production of NO ( $v = 0$  and 1) in the dissociation. The additional structure, in particular the inner rings, represent single rotational levels in the NO cofragment clearly resolved in the images. We note that only in very rare cases has rotational structure been observed in translational energy distributions using alternative detection techniques, notably in studies of van der Waals predissociation<sup>36–38</sup> and in studies relying upon the H atom Rydberg tagging technique.<sup>39</sup> In Figure 3D we directly compare the outcome of applying the usual  $\rho \sin \theta$  weighting (where  $\rho$  is the magnitude of the recoil speed and  $\theta$  the recoil direction with respect to the laser polarization direction) to both the sliced and unsliced (and reconstructed) images of  $\text{O}(^3\text{P})$  atoms from the photolysis of  $\text{NO}_2$  at 355 nm. By way of further comparison we also show the energy distribution obtained for the same system by Liu and co-workers using a core sampling time-of-flight technique that makes no use of imaging methods.<sup>40</sup> In addition to the notable increase in experimental resolution and improvement in signal-to-noise offered by the slicing approach, it is immediately apparent from this comparison is that in all three cases the energy distributions are consistent. We note that recently the Davis group at Cornell has reported results for this system using an oxygen atom-based Rydberg tagging technique.<sup>41</sup> Their results agree remarkably well with those in Figure 3, even resolving the same features seen in the DC sliced results.

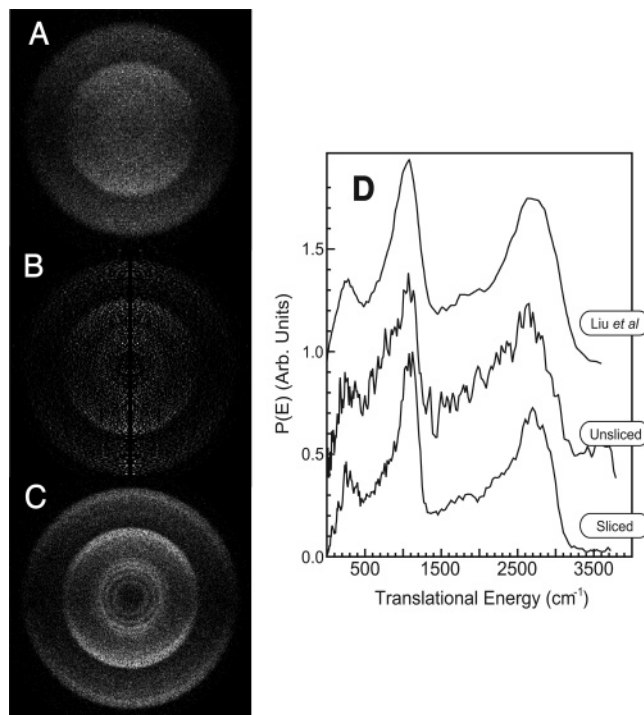


**Figure 3.** Images of  $^{16}\text{O}(^3\text{P}_2)$  from  $\text{NO}_2$  photolysis at 355 nm. (A) Unsliced; (B) reconstruction of A; (C) sliced; (D) translational energy distributions. Energy distributions for the sliced and the reconstructed images are presented along with time-of-flight core sampling data recorded by Liu and co-workers (see ref 40).

As a final illustration of the capabilities of DC slice imaging, we show results obtained with data acquisition software recently developed in our group.<sup>14</sup> In this approach, real-time centroiding of the ion image data is used to interpolate standard video to megapixel resolution. As a result, the camera itself is no longer a resolution limiting factor. Furthermore, the entire data acquisition system (camera, frame grabber and software) can be assembled for less than the cost of a personal computer. DC sliced images of D atom from DBr photodissociation at 193 nm are shown in Figure 4A. This image was obtained using 3+1 REMPI detection of the D atom, with each ion event centroided using floating point values and recorded separately. The result was then projected at 2400 by 2400 pixel resolution. The inset shows an expanded region of the recoil distribution at standard video and interpolated resolution. The velocity distribution, shown in Figure 4B, is also compared for the standard video resolution of 480<sup>2</sup> pixels along with the 2400<sup>2</sup> pixel data. The result clearly shows the improvement, with a limiting resolution of 0.5% seen for the 2400<sup>2</sup> pixel image. In this case, the excimer laser bandwidth of  $\sim 200$   $\text{cm}^{-1}$  was the dominant factor determining velocity resolution.

### III. Roaming Atoms: Reactions off the Beaten Path

We now turn from considerations of experimental enhancements to the imaging technique to applications to a range of chemical problems. The first of these examines the photoinitiated decomposition of formaldehyde, a classic system in the study of unimolecular reactions.<sup>42–46</sup>

Dissociation of energized molecules to closed-shell products generally results in large translational energy release in the fragments owing to Pauli repulsion of the electron clouds of the newly formed molecules. This repulsive interaction gives rise to a significant barrier to the reaction, and the potential energy of this exit barrier is efficiently converted to relative

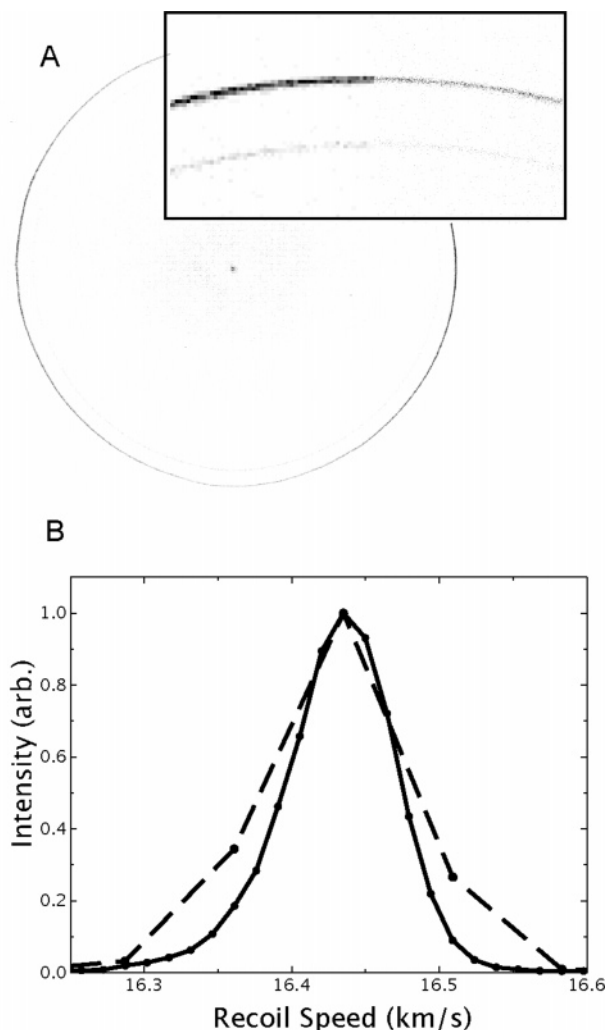


**Figure 4.** (A) D atom image from 193 nm photodissociation of DBr acquired using IMACQ megapixel imaging software. Inset shows image segment at native camera resolution compared to 5 megapixel projection. (B) D atom velocity distribution obtained at the native camera resolution (dashed line) and 5 megapixel projection (solid line).

kinetic energy of the fragments as the molecule dissociates.<sup>47,48</sup> Furthermore, the structure and vibrational frequencies of the molecule at the top of the barrier, the *transition state*, are of profound importance in determining the rate of reaction or dissociation and the thus concept of the transition state is central to the remarkably successful statistical theories of chemical reactions.<sup>49</sup> These theories began with the work of Eyring<sup>50</sup> and Evans and Polyani<sup>51</sup> in the 1930s and have evolved to Rice–Rampsberger–Kassel–Marcus (RRKM) theory and related approaches in the present day.<sup>52</sup> These theories, based upon classical statistical mechanics, assume that the transformation from reactants to products proceeds via the minimum energy pathway (i.e., over the “saddle point” in the potential energy surface) and that the rate of reaction is proportional to the ratio of the number of accessible quantum states of the transition state to the density of states of the reactants. The properties of the transition state are thus key to understanding the basis of chemical reaction rates.

The study of unimolecular dissociation of vibrationally excited molecules in the ground electronic state has been central to the development these theories,<sup>53,54</sup> and formaldehyde has become a classic example<sup>55</sup> with which to study these issues. It is one of the simplest molecules in which to explore the correlation between internal excitation in both products; it is straightforward

to use laser excitation to prepare molecules on the ground electronic state with specific amounts of internal energy. Specifically, excitation to a single rovibrational level of the bound first excited electronic state,  $S_1$ , is followed by rapid internal conversion (IC) back to the ground state,  $S_0$ . The vibrationally excited  $H_2CO$  can then dissociate on the ground state potential surface, and two possible unimolecular decomposition pathways are known to take place: A lower energy molecular elimination channel forming  $CO + H_2$  (transition state energy  $\sim 28\,600\text{ cm}^{-1}$ ) and a higher energy ( $> 30\,300\text{ cm}^{-1}$ ) radical channel giving rise to  $H + HCO$ . In pioneering experiments spanning more than a decade, Moore and co-workers examined the unimolecular reaction dynamics of formaldehyde in great detail.<sup>42,44–46,56,57</sup> They studied both  $H_2$  and  $CO$  product state distributions and state-resolved  $H_2$  Doppler profiles; among their findings were a hot  $CO$  rotational distribution but cold  $CO$  vibrational distribution, modest  $H_2$  vibrational excitation, and cold  $H_2$  rotational distributions. In addition, they reported  $\sim 65\%$  of the available energy is partitioned into translation. These observations could be accounted qualitatively by the nature of the well-documented “skewed” transition state structure,<sup>58</sup> and in fact, the details allowed for characterization of the transition state properties and insight into the exit channel dynamics.<sup>59,60</sup>

However, one significant feature of the measurements did not fit well with this simple picture of the unimolecular dissociation dynamics: van Zee et al. noted<sup>46</sup> that when formaldehyde was excited at energies above the threshold for dissociation to  $H + HCO$ , the  $CO$  rotational distributions exhibited an anomalous shoulder to lower rotational levels. They proposed two possible explanations for this low- $j_{CO}$  component. One was that at higher energies a degree of anharmonic motion at the transition state could lead to dissociation from small impact parameter geometries, so that little rotational excitation might be produced in the  $CO$ . The second possibility was that the low  $j_{CO}$  was directly related to the opening of the radical dissociation channel and a distinct new pathway to formation of molecular products. The latter possibility is of particular interest in that there have recently emerged a handful of examples of reactions that do not involve transition state structures at all.<sup>61–65</sup> These reactions challenge conventional transition state theories and raise many important questions: Can these intramolecular abstraction pathways exist in competition with conventional transition state pathways? How common are these alternative mechanisms? Can they involve products other than  $H_2$ ?

We performed high-resolution DC slice imaging measurements of specific  $CO$  rovibrational levels following dissociation of formaldehyde both below and above the threshold for the radical channel.<sup>66</sup> These images provide the *correlated*  $H_2$  internal energy distributions with vibrational and partial rotational resolution. The experimental images and the translational energy distributions obtained from the images are shown in Figure 5. Images recorded on high  $CO$  rotational levels, near the peak of the rotational state distribution, show formation of the correlated  $H_2$  in low vibrational levels ( $v = 0–4$ , peaking at  $v = 1$  or  $2$ ), and this is the case for excitation below the  $H + HCO$  threshold, recorded on the  $2^1_41$  band (Figure 5A), as well as above it (Figure 5B), recorded on the  $2^1_43$  band. Dissociation below the threshold, however, yields almost no population in low rotational levels of  $CO$ , so data for low  $j_{CO}$  following excitation on the  $2^1_41$  band could not be obtained. For dissociation on the  $2^1_43$  band, above the  $H + HCO$  threshold, we obtain the images in Figure 5B–D. For  $j_{CO} = 28$

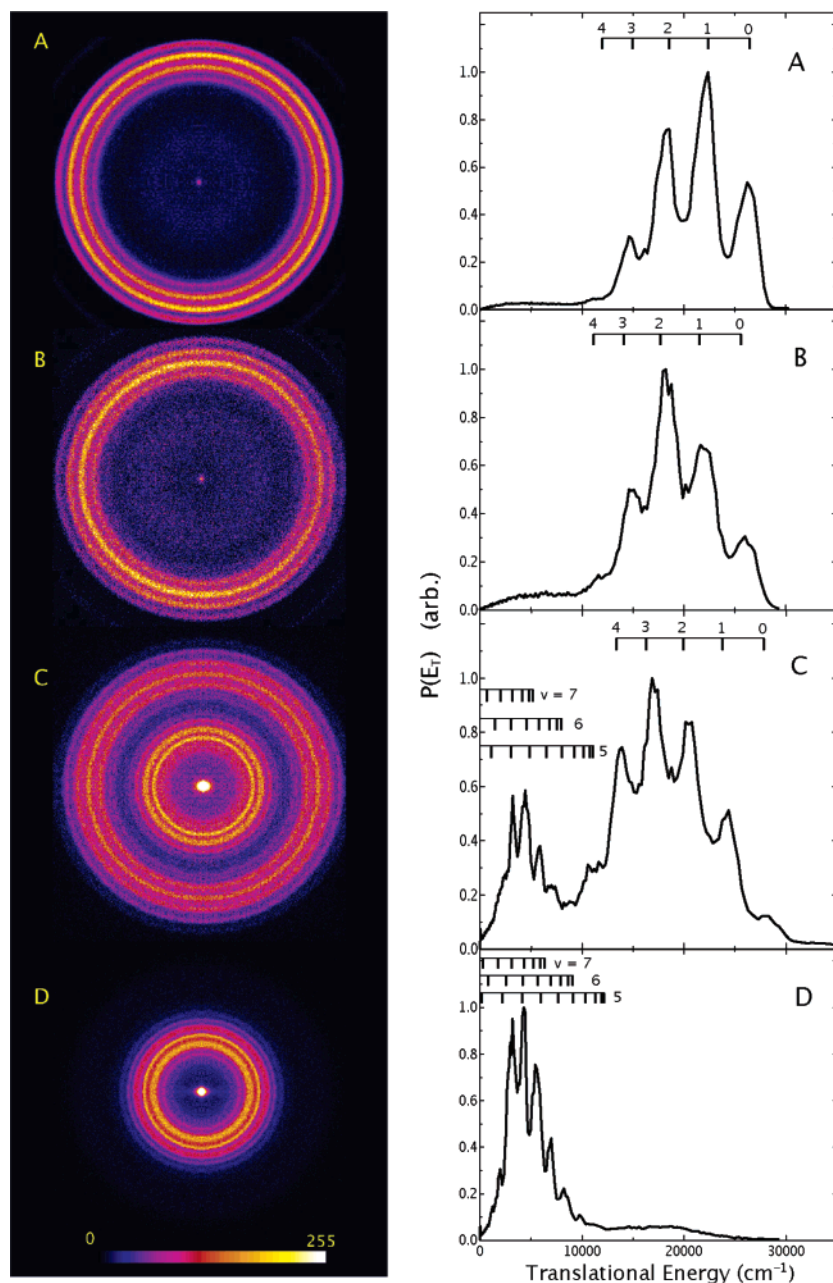


**Figure 5.** Left: DC sliced images of CO for dissociation of  $\text{H}_2\text{CO}$  on the  $2^14^1$  band (A) and  $2^14^3$  band (B)–(D) for  $j_{\text{CO}} = 40$  (A, B),  $j_{\text{CO}} = 28$  (C), and  $j_{\text{CO}} = 15$  (D). Right: Translational energy distributions obtained from the corresponding images at left. Markers indicate correlated  $\text{H}_2$  vibrational levels for  $j_{\text{H}_2} = 5$  (for  $v = 0-4$ ) or rovibrational levels (for  $v = 5-7$ ).

(Figure 5C), which is intermediate between the peak of the rotational distribution and the low- $j_{\text{CO}}$  shoulder reported by van Zee et al., the image shows a bimodal internal energy distribution in the  $\text{H}_2$  co-product, strongly suggesting two distinct dissociation mechanisms. The corresponding translational energy distribution, showing partial rotational resolution of the correlated  $\text{H}_2$ , reveals that the slower CO ( $v = 0$ ,  $J = 28$ ) product is formed in conjunction with  $\text{H}_2$  in vibrational levels up to  $v = 7$ . Finally, the image in Figure 5D, recorded by probing CO ( $v = 0$ ,  $J = 15$ ), shows only the slow component, and the translational energy distribution reveals that it is quite similar to the slow part of the distribution of Figure 5C. We see only formation of highly internally excited  $\text{H}_2$  in conjunction with CO ( $v = 0$ ,  $J = 15$ ), again up to  $v = 7$ ,  $J = 11-13$   $\text{H}_2$ .

As discussed previously, in the original work of van Zee et al., two possible mechanisms were proposed to account for the low- $j_{\text{CO}}$  product: (1) anharmonic motion at the transition state

leading to reduced exit impact parameters; (2) low- $j_{\text{CO}}$  product resulting from a distinct pathway to molecular products related to the  $\text{H} + \text{HCO}$  dissociation channel, i.e., an intramolecular H abstraction process. Our results strongly support the latter hypothesis, also the one favored by van Zee et al. The very large vibrational excitation in the coincident  $\text{H}_2$  would not be expected for the former mechanism, yet it is just what one might expect to see resulting from the  $\text{H} + \text{HCO}$  hydrogen abstraction reaction. Highly convincing support for this notion comes from QCT calculations performed by the Bowman group.<sup>66,67</sup> The calculations reproduce the state correlations in translational energy distributions quite well, but more, they enable one to follow individual trajectories to gain insight into the dynamics. Several frames of one trajectory leading to  $\text{H}_2$  in  $v = 6$  and CO in  $j_{\text{CO}} = 11$  are shown in Figure 6. Here, it is seen that the reaction proceeds first by near loss of a hydrogen atom followed by “roaming” of this hydrogen atom in the broad attractive space

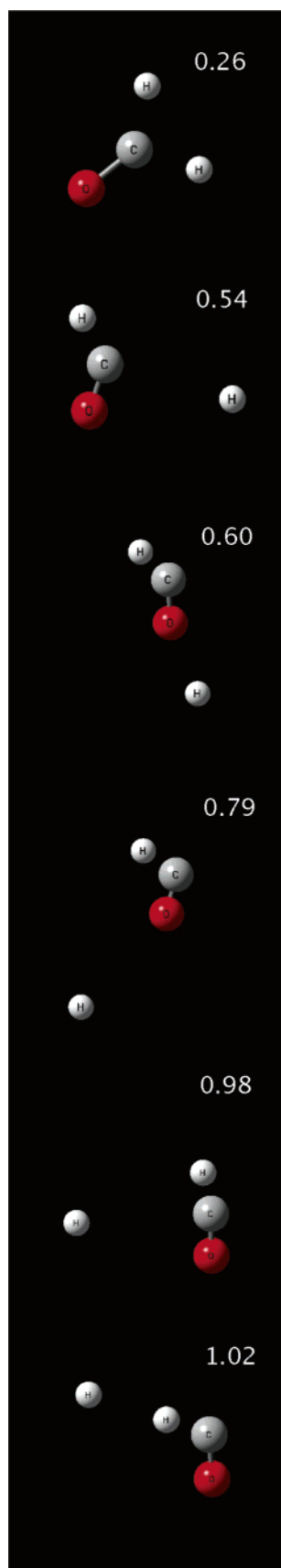


**Figure 6.** Snapshots of sample trajectory leading to  $j_{\text{CO}} = 6$  and  $\text{H}_2$   $v = 7$  showing roaming mechanism (adapted from ref 66). Time (in picoseconds) is shown for each snapshot.

of the  $\text{H} + \text{HCO}$  potential. The roaming atom aligns itself with the remaining H atom in a nearly linear C–H–H geometry at

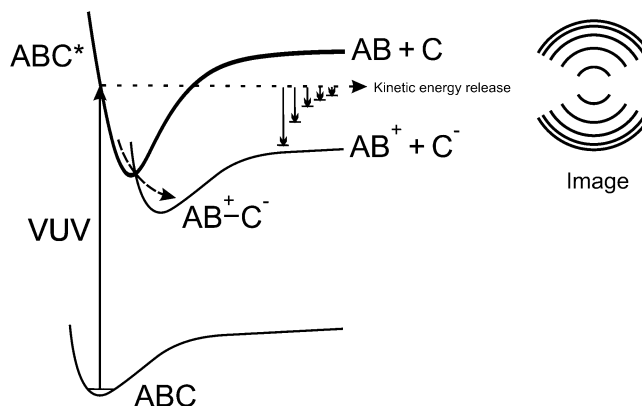


**Figure 7.** Schematic representation of the IPIS technique

an extended H–H distance, then reaction occurs to form highly vibrationally excited  $\text{H}_2$  and rotationally cold CO. These results challenge conventional transition state theory notions for a number of reasons. One, this is a reaction that completely avoids the well-known region of the transition state. Although reactions at high energy commonly do not follow the minimum energy path, this mechanism is quite distinct in that it involves successive near-dissociation via the H elimination channel followed by intramolecular abstraction through another barrierless process. Second, because it involves near-loss of the hydrogen atom, it is in some sense a re-crossing process. Perhaps most significant is the fact that this may not be at all unusual: there is nothing extraordinary about formaldehyde that makes this particularly likely. An important direction for us now is to investigate how general this phenomenon may be.

We also note additional details revealed by these state-correlated measurements. An examination of the translational energy distributions in Figure 5, even for the “nonroaming” mechanism giving rise to  $\text{H}_2$  ( $v = 0\text{--}4$ ), shows a significant dependence of the  $\text{H}_2$  vibrational distribution on both the CO rotational level with which it is correlated and the precise excitation energy. These details are very sensitive to the features of the transition state and the exit channel dynamics and are the subject of current investigation.

#### IV. Ion Pair Imaging

We have recently pursued an alternative strategy for the study of ion spectroscopy and excited state decay dynamics using velocity map imaging to probe *ion pair* formation processes.<sup>18,68,69</sup> Ion pair dissociation usually represents one of several decay channels for superexcited states, i.e., highly excited neutral states lying above the ionization potential of the molecule.<sup>70,71</sup> The approach, schematically illustrated in Figure 7, is analogous to photoelectron imaging, but one in which a halide anion plays the role of a “heavy electron”. This technique has several advantages that make it useful in some cases in which traditional ion spectroscopy methods are impractical. For example, ion pair imaging of stable molecules gives rise to ions that would be produced by direct photoelectron spectroscopy of a radical precursor. In addition, because this is a slower process than direct ionization, Franck–Condon constraints are greatly relaxed relative to photoelectron spectroscopy or direct absorption. A clear shortcoming is that the technique relies upon access to ion pair potential surfaces via Rydberg states that can be optically excited and that do not decay strongly through other pathways. This is by no means a universal situation. Finally, we note that Kawasaki and co-workers were the first to report



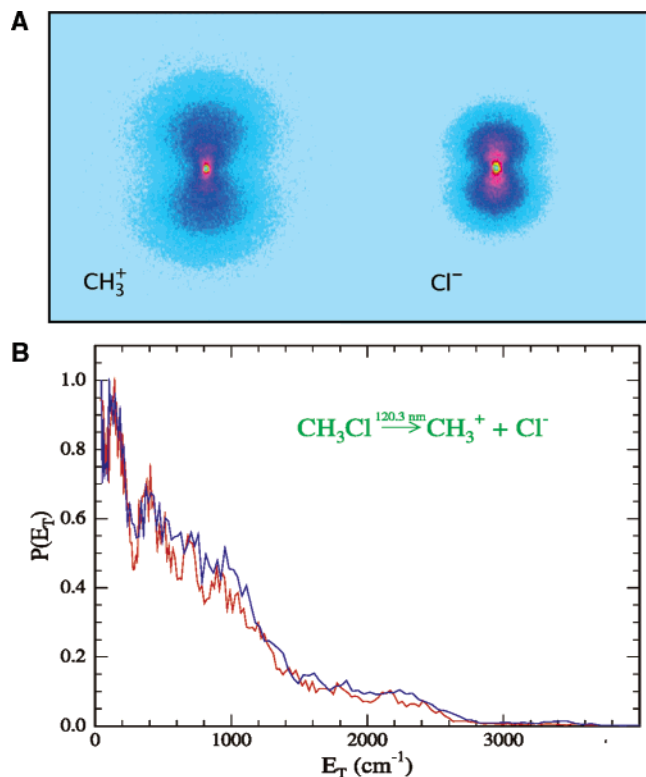


**Figure 8.** (A) Ion pair images of methyl chloride at 120.3 nm. (B) Total translational energy distributions obtained from  $\text{CH}_3^+$  (red) and  $\text{Cl}^-$  (blue) images in A.

ion pair imaging, in a study that pre-dated velocity mapping and was directed to probing the dynamics of the process rather than obtaining spectroscopic information.<sup>72</sup>

In Figure 8 we present results for ion pair imaging spectroscopy (IPIS) of methyl chloride at 120.3 nm showing images for the methyl cation and the chloride anion. We may use either fragment to reconstruct the total translational energy distribution, and these are also compared in Figure 8. The agreement shows that we are indeed detecting momentum-matched fragments from an ion pair dissociation process. These images do not show very good signal-to-noise because both the VUV laser was not particularly intense at this wavelength and the ion pair dissociation cross section is not large here near threshold. DC slice imaging results obtained at 118 nm, Figure 9, show greatly improved resolution and signal-to-noise. The associated translational energy distribution exhibits single rotational level resolution and a progression in the  $\nu_2$  umbrella mode and a combination band involving  $\nu_4$ . The latter has been inferred from nuclear spin statistics and simulations of the rotational structure. We have fitted these peaks to obtain these two vibrational frequencies as well as experimental estimates of the rotational constants.<sup>69</sup>

Although the example we have presented shows the use of ion pair imaging as a probe of ion spectroscopy, it can also be used to explore the detailed dynamics of superexcited state decay processes. We direct the interested reader to one such study, in which we have used a VUV free electron laser at Brookhaven National Laboratory to study ion pair formation dynamics in methyl fluoride at  $\sim 14$  eV.<sup>18</sup> This study revealed the complex multistep dynamics involving superexcited state preparation, internal conversion to lower Rydberg states, then Rydberg–ion pair surface couplings leading to dissociation.

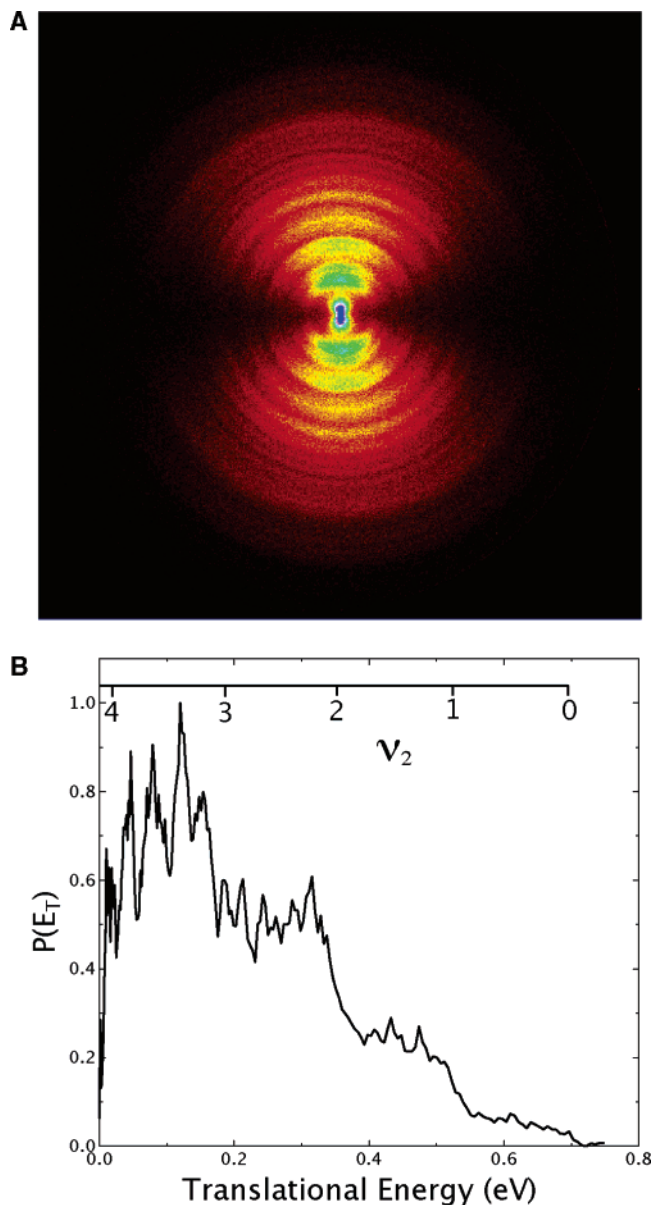


**Figure 9.** (A) DC sliced ion pair image of methyl chloride at 118. (B) Translational energy distribution obtained from image.

## V. Reactive Scattering

Although photochemistry provides the opportunity to isolate a system and study its behavior at precise energies, real chemistry involves collisions. Collision experiments are thus key to probing the fundamental aspects of genuine chemical encounters. In these experiments we ask questions such as: What are the initial products and their internal states? How is the energy of the collision or the reaction partitioned into these products in rotation, vibration or electronic excitation? What is the fate of the angular momentum? What parts of the molecule are most reactive? What influence does anisotropy of the potential have, or shallow van der Waals wells? What influence does the initial energy (translational, rotational, vibrational, electronic) have on the reaction outcome? The answers to these questions reveal the most intimate details of the interaction and allow us to sharpen our chemical intuition. As an example, we will contrast the dynamics of the reaction of ground state and electronically excited oxygen atoms with *n*-pentane obtained in an imaging crossed-beam experiment.<sup>73</sup>

In this experiment, a beam of *n*-pentane is directed toward the imaging detector, parallel to an  $\text{SO}_2$  or  $\text{N}_2\text{O}$  beam that is

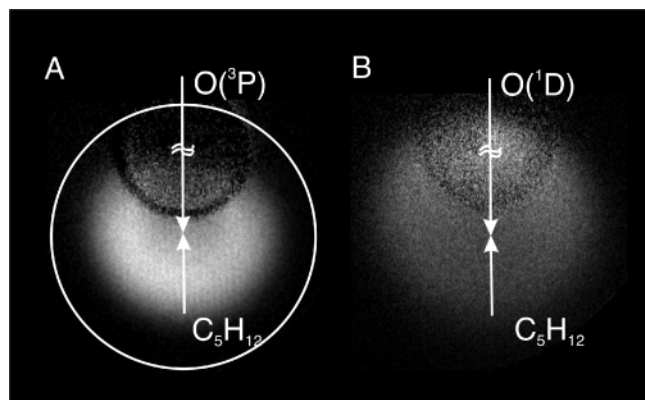


**Figure 10.** C<sub>5</sub>H<sub>11</sub> images from O + *n*-pentane reaction: (A) reaction of O(<sup>3</sup>P); (B) reaction of O(<sup>1</sup>D). Subtraction of photochemistry background gives rise to “ghost” at pentane beam velocity.

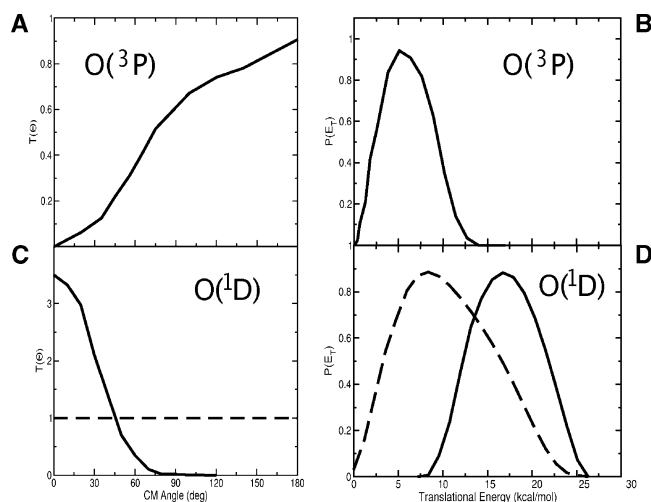


**Figure 11.** Angular (A, C) and translational energy (B, D; right) distributions for the indicated O atom reactant obtained from the images in Figure 11 by Monte Carlo forward convolution fitting. (A) and (B) correspond to O(<sup>3</sup>P) reaction; (C) and (D) correspond to O(<sup>1</sup>D) reaction. Dashed lines in (C) and (D) correspond to isotropic contribution to the fit.

used to generate the oxygen atom beam (for O(<sup>3</sup>P) and O(<sup>1</sup>D), respectively.) Oxygen atoms react with pentane to produce OH + pentyl radicals. The latter are detected with great sensitivity by “universal” single photon ionization using a VUV 157 nm F<sub>2</sub> excimer laser.<sup>74</sup>

The resulting reactively scattered pentyl radical images (Figure 10) are analyzed using a Monte Carlo forward convolution program<sup>17</sup> to yield the detailed translational energy and angular distributions (Figure 11). Reaction of ground state oxygen atoms shows a backward scattered angular distribution: that is, the pentyl radical product is scattered back (in the center of mass frame) in the direction of the pentane beam origin. This indicates a direct reaction mechanism. Furthermore, little of the reaction exothermicity appears in product translational energy, and this has been ascribed to vibrational excitation in the radical owing to the difference between the parent and the radical equilibrium geometries. When we consider reaction of O(<sup>1</sup>D), with an additional 2 eV available energy, we find strikingly different behavior. In this case, the product distributions are analyzed in terms of two distinct components because there is a strong dependence of the translational energy distribution on the angular distribution. The forward scattered component is faster than the sideways or backward distribution,

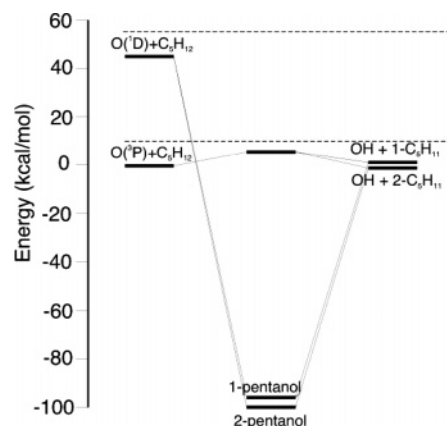


**Figure 12.** Stationary points on O + *n*-pentane potential surfaces.

so it is fitted separately, with the remainder fitted as an isotropic distribution. The nature of the interaction is clearly very different for the O(<sup>1</sup>D) reaction. Here, there is no barrier for insertion of O(<sup>1</sup>D) into the C–H bond to form the alcohol, and there is a very deep potential well associated with this intermediate (Figure 12). We thus expect a long-lived complex giving rise to forward–backward symmetry in the angular distribution: this is the isotropic component. But what is the source of the forward scattering? On the basis of OH product state distributions obtained by the Wiesenfeld group,<sup>75</sup> and supported by recent direct dynamics calculations for the analogous O(<sup>1</sup>D) + CH<sub>4</sub> reaction,<sup>76</sup> it has long been suspected that there is both a statistical component associated with insertion and a transient intermediate that lives perhaps only a few OH vibrational periods at most. In these imaging experiments, we can associate the forward scattered product with nonstatistical decay of the transient intermediate and greater translational energy release, and we associate the isotropic component with fully statistical decomposition of the long-lived insertion intermediate.

The starkly contrasting dynamics in these two parallel systems show that total energy may be a small part of the story. When we add 2 eV additional energy into the system by going from the O(<sup>3</sup>P) to the O(<sup>1</sup>D) reaction, we find the counterintuitive change from direct dynamics to a long-lived intermediate. Of course we have done more than simply add energy to the system when we switch to the O(<sup>1</sup>D) reaction; we have changed from the triplet potential energy surface (see Figure 12), which has a barrier but no significant well, to the singlet surface which has no barrier but a very deep well. It is the topology of the potential energy surface rather than the total energy that governs the dynamics.

## VI. Orbital Polarization in Photodissociation

It has long been known that orbital polarization of atomic photofragments may occur when molecular photodissociation is initiated by polarized light.<sup>77,78</sup> Although early experimental investigations of this phenomenon reported only the total net orbital angular momentum polarization, more recent studies have focused on the *recoil angle dependence* of this effect. This is the electronic **v**–**J** vector correlation and an understanding of this phenomenon may provide a deep insight into the nature of the potential energy surfaces on which the dissociation event takes place, as well as the couplings between them. One of the great strengths of imaging approaches, and in particular the slice imaging technique introduced previously in this article, is that they can readily reveal the angular distribution of the angular momentum polarization. In a series of papers in collaboration with the Vasyutinskii group,<sup>19,79,80</sup> our group has established

the connection between imaging measurements and the detailed angular momentum dynamical functions introduced by Siebbeles et al.<sup>81</sup> These functions decompose the electronic  $\mathbf{v}-\mathbf{J}$  correlation into both incoherent and coherent contributions arising from excitation of parallel and perpendicular electronic transitions. The measurements may then be used to understand the nature of the dissociation dynamics, the contributions from nonadiabatic processes and curve crossings, the shape and angular dependence of the atomic charge cloud in the recoiling atomic photo-fragment, and the influence of long-range potential interactions. The detailed theoretical treatment of these phenomena for polyatomic molecules, however, is just in its infancy, and this work is actively being pursued in a number of laboratories.<sup>30,31,82–85</sup>

Polarization effects are generally expressed either as *orientation*, corresponding to cases in which populations of magnetic sublevels  $\pm m_J$  have unequal populations (probed using circularly polarized light), or *alignment*, in which populations in different  $|m_J|$  levels differ (probed using linearly polarized light). It should be noted here that  $m_J$  refers to the projection of the total photofragment angular momentum,  $J$ , onto the axis defined by the breaking bond in the molecule undergoing dissociation and that within the theoretical treatment that will be outlined here it is assumed that this bond breaks on a time scale significantly faster than the period of molecular rotation—the so-called axial recoil approximation. Moments of the  $m_J$  angular momentum distribution exist, up to rank  $K = 2J$ , where  $J$  is the total angular momentum of the photofragment species under investigation, and to date, a rigorous, fully quantum mechanical treatment has been developed for the  $K = 1, 2$  and 4 moments.<sup>86–88</sup>

The state multipoles that define the moments of each rank  $K$  may be expressed in terms of a series of anisotropy basis functions. Each function describes a characteristic angular distribution resulting from a distinct dynamical processes taking place during the dissociation event. Within this treatment the *orbital polarization anisotropy* in the experimental images is isolated from the *population anisotropy* by subtracting signals recorded under different polarizations of the probe laser. The former is a result of variations in the photofragment  $m_J$  distribution as a function of recoil angle and the associated change in ionization probability for a given *probe* laser polarization, and the latter effect is caused by the interaction between the *photolysis* laser and the transition dipole moment of the molecule under study—as characterized by the well-known expression  $I(\theta) = 1 + \beta P_2(\cos \theta)$ , where  $P_2$  is the second Legendre polynomial. The polarization anisotropy basis functions specific to the case of slice imaging for the  $K = 1$  and 2 moments have been recently derived by our group, on the basis of the original formalism used by Vasyutinskii and co-workers to describe the complete 3D basis distribution.<sup>79,80,86</sup> A detailed discussion is beyond the scope of this article; however, the final form of the functions describing the image anisotropy arising from each distinct dissociation mechanism are plotted in Figure 13.

We present ozone photodissociation at 266 nm as an illustration of this approach.<sup>80</sup> DC sliced images of ozone photodissociation obtained with linearly polarized photolysis and probe lasers (Figure 14) are combined to eliminate the population contribution and reveal the alignment distribution exclusively. Note that the four rings in each image correspond to production of  $v = 0-3$  in the  $O_2(a^1\Delta_g)$  cofragment. Analysis of the alignment image then gives the speed-dependent anisotropy parameters that contain dynamical information relating to the dissociation event. In this instance, we find the alignment

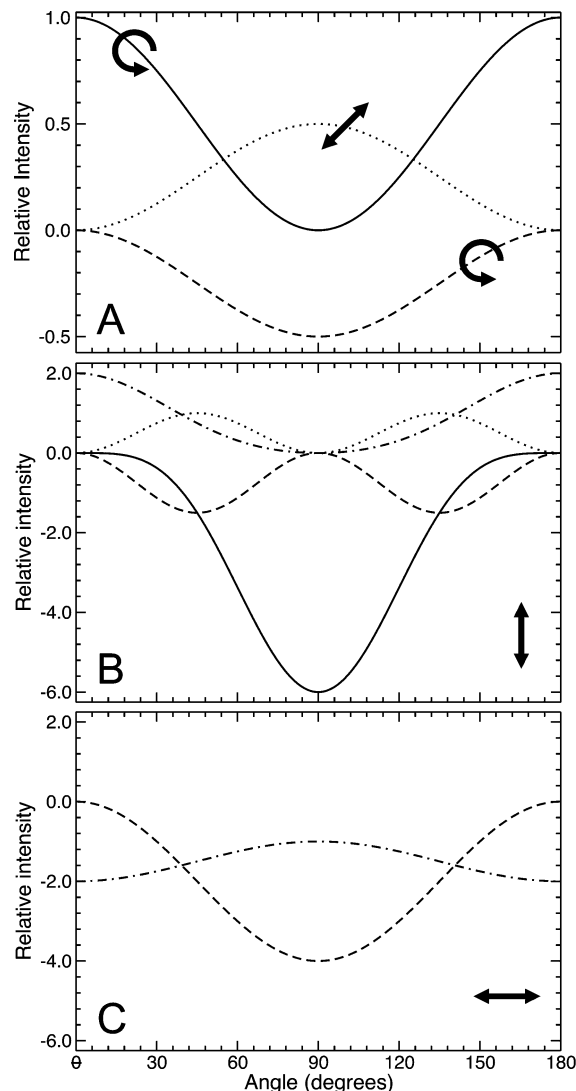


**Figure 13.** Slice imaging polarization anisotropy basis functions. Arrows indicate photolysis laser polarization. (A)  $K = 1$  (orientation): incoherent perpendicular ( $\alpha_1$ ) resulting from circular photolysis (solid line), coherent perpendicular and parallel ( $\gamma_1$ ) resulting from circular photolysis (dashed line), coherent perpendicular and parallel ( $\gamma_1'$ ) resulting from linear photolysis (dotted line). (B), (C)  $K = 2$  (alignment): incoherent parallel ( $s_2 = -\alpha_2$ ) (solid line), incoherent perpendicular ( $s_2 = 2\alpha_2$ ) (dashed line), coherent perpendicular and parallel ( $\gamma_2$ ) (dotted line), coherent perpendicular and parallel ( $\eta_2$ ) (dot-dash line). Note that an angle of  $90^\circ$  corresponds to vertical in the difference images shown in other figures. A more detailed description of the coordinate system may be found in ref 80.

is quite substantial and results largely from an incoherent parallel excitation mechanism, which is largely invariant with photofragment recoil energy. The electronic charge cloud distribution associated with the O-atom recoiling axially along the axis of the breaking bond (averaged over all recoil energies) is shown in Figure 15, and this corresponds to a density matrix dominated by the  $m_J = 0$  ( $\mathbf{J}$  perpendicular to  $\mathbf{v}$ ) diagonal element (also shown), consistent with previous measurements by Houston and co-workers.<sup>83</sup> Note that the polarization of the photolysis laser is directed along the Z-axis in this instance and that, although fragments recoiling perpendicular to this direction display a propensity for  $m_J = \pm 2$  ( $\mathbf{J}$  parallel to  $\mathbf{v}$ ), only a small number of O-atoms are initially scattered in this direction, as characterized by the recoil anisotropy parameter,  $\beta \sim 1.2$ .<sup>83</sup>

Although the polarization is likely to be dominated by the low-order,  $K = 1, 2$  moments, higher moments exist



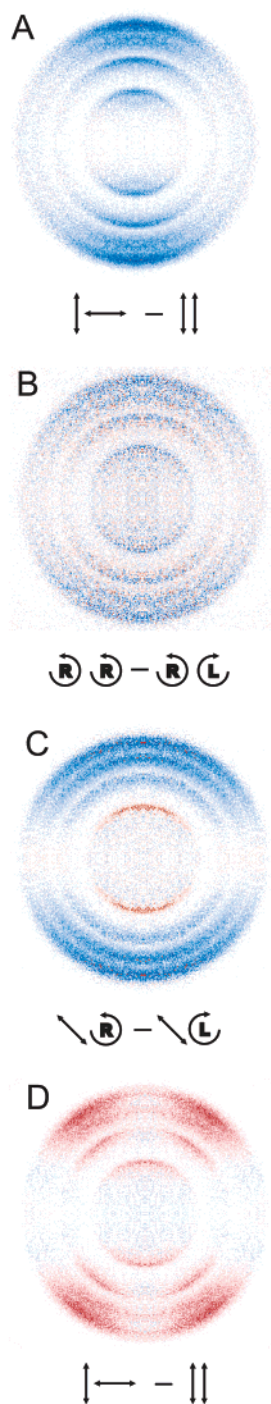


**Figure 14.** DC sliced difference images of O ( $^1D_2$ ) atoms from the photolysis of ozone at 266 nm recorded using different combinations of REMPI probe transition and/or pump–probe polarization geometry. Each pair of arrows denotes the polarization of the photolysis (LHS) and probe (RHS) lasers. Blue and red correspond to positive and negative intensities, respectively. Images were obtained using REMPI probe on the  $^1F_3$  transition (A) or  $^1P_1$  transition (B)–(C) (see text).

and may be necessary to characterize the dynamics fully. Such moments are not explicitly considered in our current alignment analysis because the REMPI probe scheme used to record the difference image in Figure 14A only exhibits a weak sensitivity to them (see refs 19 and 89 for a detailed description). As can be seen in Figure 14D, by probing the O-atoms produced in the dissociation using a different REMPI scheme (one that has a much higher sensitivity to such rank 4 moments), the presence of this contribution is more readily revealed (as characterized

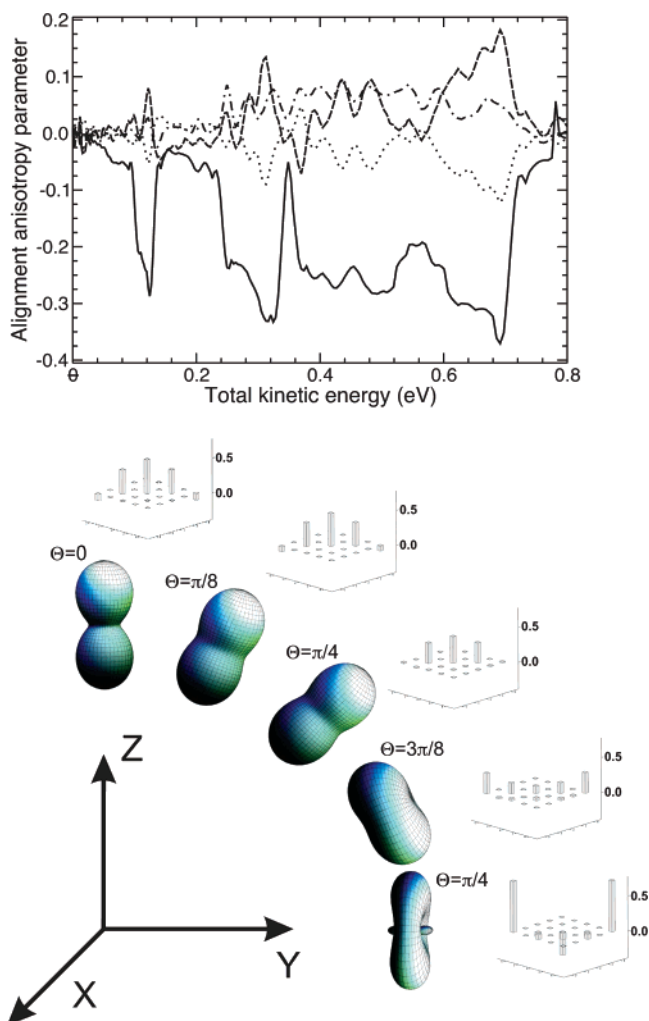


**Figure 15.** (Top) rank 2 alignment anisotropy parameters as a function of O ( $^1D_2$ ) atom kinetic energy following the photodissociation of ozone at 266 nm. Incoherent parallel ( $s_2 = -\alpha_2$ ) (solid line), incoherent perpendicular ( $s_2 = 2\alpha_2$ ) (dashed line), coherent perpendicular and parallel ( $\gamma_2$ ) (dotted line), coherent perpendicular ( $\eta_2$ ) (dot–dash line). (Bottom) electron charge cloud distributions in the recoiling of O ( $^1D_2$ ) atom obtained from the parameters in the above plot (averaged over all recoil energies) at five different recoil angles. Also shown are plots of the density matrices describing the associated  $m_J$  distribution in each case.

by the four lobes in the difference image). The presence of these higher order effects indicates the role of other contributions to the dissociation dynamics, and work is currently underway in our group to analyze these results in more detail.

By employing a circularly polarized REMPI laser, we can probe the angular momentum *orientation* in the product atom. This can provide another route to insight into the dissociation dynamics that may not be apparent from considering the rank 2 alignment alone. Orientation may arise from dissociation by circularly polarized light, in which case it is a manifestation of the helicity of the dissociation photon propagating into the product polarization, or it can be induced by photodissociation by linearly polarized light (set at  $45^\circ$  with respect to the imaging plane; for a detailed discussion see ref 87), in which case it is a consequence of coherent parallel and perpendicular contributions to the dissociation dynamics.<sup>81,90,91</sup> In the case of ozone dissociation at 266 nm, the contributions from the former mechanism, involving photolysis by circularly polarized light, are negligible within the statistical error, as can be seen in Figure 14. However, the O ( $^1D_2$ ) orientation induced by linearly



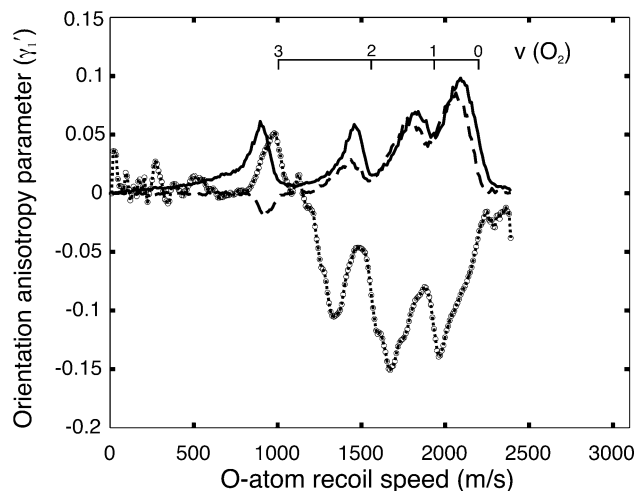


**Figure 16.** Rank 1 orientation anisotropy parameter,  $\gamma_1'$ , as a function of O ( $^1\text{D}_2$ ) atom recoil speed following the photodissociation of ozone at 266 nm. The circles correspond to  $\gamma_1'$ , and the solid and dashed lines denote the total population and the difference signal, respectively. These latter two plots have been scaled arbitrarily.

polarized photolysis at  $45^\circ$  is strong and shows a striking recoil-speed dependence (Figure 14C). The absolute  $K = 1$  orientation parameter quantifying the extent of this effect may be obtained by fitting the (normalized) difference image in Figure 14C with the relevant basis functions (plotted in Figure 13). The result is shown in Figure 16. For the fast peaks, corresponding to coincident production of  $\text{O}_2$  ( $\text{a}^1\Delta_g$ ) in  $v = 0-2$ , the orientation is large and positive. However, for the slowest peak ( $v = 3$ ), the orientation actually changes sign. Furthermore, close inspection of the speed dependence for each vibrational peak reveals that the maximum orientation does not coincide with the maximum rotational population associated with each vibrational level. Instead, maximum orientation occurs to high  $J$  for  $v = 0-2$  and to low  $J$  for  $v = 3$ . This, and the wavelength dependence of the orientation, have been studied in some detail and used to reveal, in ozone, two distinct pathways to the same product that are coherently excited via a single state.<sup>80</sup>

As a final demonstration of the advantage slice imaging offers over “forward convolution” methods in the study of strongly recoil-speed dependent orbital polarization, we compare directly the results obtained for ozone photodissociation under sliced

and unsliced conditions at a photolysis wavelength of 248 nm. Experimental difference images recorded when probing the  $K = 1$  moment using linearly polarized light are shown in Figure 17. At this wavelength, the formation of  $v = 0-5$  is energetically allowed in the  $\text{O}_2$  cofragment, and in the sliced image, five out of the six rings are clearly visible ( $v = 0$  and 1 are not fully resolved). Also shown in Figure 17 is the theoretical difference image that is expected in the unsliced case in instances when a strong coherent interaction between perpendicular and parallel dissociation mechanisms is present (i.e., the result of compressing the entire 3D basis function describing such an effect onto 2D).<sup>87</sup> It is important to note here that this theoretical “basis image” only represents the case of a monoenergetic photofragment energy release. The unsliced experimental image may therefore be regarded as a superposition of many such basis images, each of a different diameter (corresponding to each different fragment release energy) and a different “intensity” (related to the magnitude of the orientation effect in each case). Although it is immediately clear from the experimental sliced image that both the sign and magnitude of the orientation effect changes profoundly as a function of O-atom recoil speed, such information (in particular, the most subtle features, such as the shift in the orientation maximum relative to the population maximum) will clearly be much more difficult to obtain from the unsliced case using forward convolution of the data. Furthermore, this problem will be further compounded in situations where multiple dissociation mechanisms (i.e., multiple basis images) contribute to the total observed orbital polarization at each recoil energy, as is often the case when  $K \geq 2$  moments are considered.

## VII. Summary and Outlook

We have highlighted the use of high-resolution ion imaging, in particular DC slice imaging, to address a broad range of fundamental problems in chemical reaction dynamics. Examples drawn from our recent work include applications in state-correlated photodissociation, ion pair dissociation dynamics and spectroscopy, crossed-beam reactive scattering, and atomic orbital polarization in photodissociation. Although the focus has been on results from our laboratory, we note with pleasure that ion imaging methods are gaining many new converts, with new approaches appearing in femtosecond photoelectron spectroscopy,<sup>92</sup> photoelectron-photoion coincidence techniques<sup>93</sup> and ion photochemistry.<sup>94</sup>

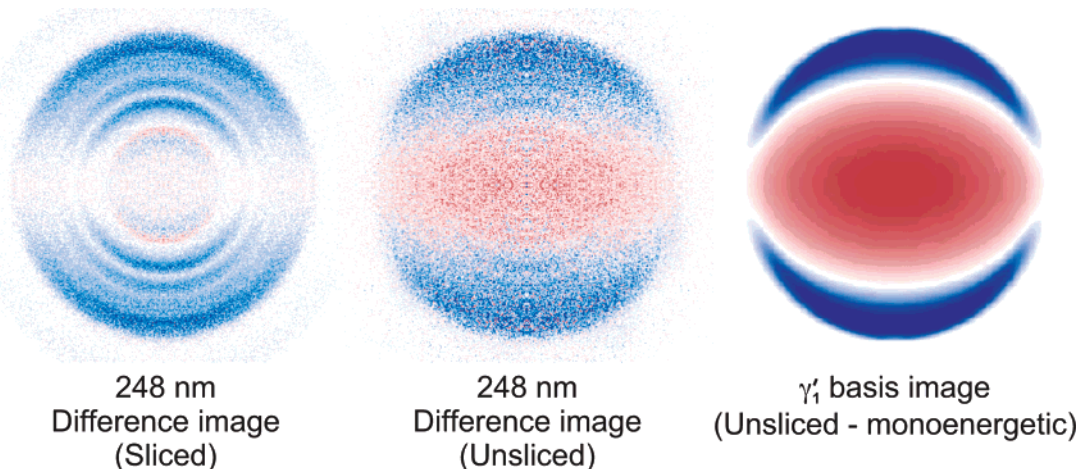


**Figure 17.** Difference images of O ( $^1\text{D}_2$ ) atoms from ozone dissociation at 248 nm recorded under sliced and unsliced conditions using a linearly polarized photolysis laser (at  $45^\circ$  to the detection plane) and a circularly polarized probe. Blue and red correspond to positive and negative intensities, respectively. Also shown is the 2D difference basis image predicted when a strong coherent interaction exists between perpendicular and parallel dissociation pathways.<sup>87</sup>

The field of chemical dynamics itself is quite robust, with many active areas of current investigation beyond the scope of what has been presented here. Exciting avenues are being pursued in coherent and shaped-pulse control of reactive outcomes;<sup>95,96</sup> spectroscopy and dynamics in ultracold helium droplets; novel spectroscopies using femtosecond lasers;<sup>97,98</sup> chemically sensitive microscopies<sup>99</sup> and single-molecule techniques;<sup>99</sup> and tabletop and free-electron laser approaches to time-resolved X-ray studies in the femtosecond<sup>100</sup> and even attosecond regime.<sup>101</sup> With the remarkable versatility and ongoing improvements in imaging techniques, we may be confident of exciting new applications in these emerging areas.

**Acknowledgment.** This work reflects the contributions of many students, post-docs and collaborators over the years. In particular, we acknowledge M. Ahmed, D. S. Peterka, X. Liu, M. Minitti, M. Kim, P. Hallock, S. Lahankar, S. Chambreau, B. Leskiw, O. S. Vasyutinskii, J. M. Bowman, and G. E. Hall and the Gas Phase Dynamics Group at BNL. This work was supported by the Director, Office of Science, Office of Basic Energy Sciences, Division of Chemical Sciences, Geosciences and Biosciences, of the U.S. Department of Energy under contracts DE-AC02-9810886 (BNL) and DE-FG02-04ER15593 (WSU) and by the National Science Foundation under grants CHE-0102174 (SBU) and CHE-0415393 (WSU). Additional support was provided by the US-CRDF under award RC2-2570-ST-03.

## References and Notes

- Levine, R. D. *Molecular Reaction Dynamics*; Cambridge University Press: Cambridge, U.K., 2005.
- Lee, Y. T. *Science* **1987**, 236, 793.
- Shafer, N. E.; Orreling, A. J.; Simpson, W. R.; Xu, H.; Zare, R. N. *Chem. Phys. Lett.* **1993**, 212, 155.
- Valentini, J. J. *Annu. Rev. Phys. Chem.* **2001**, 52, 15.
- Schnieder, L.; SeekampRahn, K.; Wrede, E.; Welge, K. H. *J. Chem. Phys.* **1997**, 107, 6175.
- Wrede, E.; Schnieder, L.; Welge, K. H.; Aoiz, F. J.; Banares, L.; Castillo, J. F.; Martinez-Haya, B.; Herrero, V. J. *J. Chem. Phys.* **1999**, 110, 9971.
- Lin, J. J.; Zhou, J. G.; Shiu, W. C.; Liu, K. P. *Science* **2003**, 300, 966.
- Valentini, J. J. *Annu. Rev. Phys. Chem.* **2001**, 52, 1539.
- Zewail, A. H. *J. Phys. Chem. A* **2000**, 104, 5660.
- Neumark, D. M. *Phys. Chem. Chem. Phys.* **2005**, 7, 433.
- Chandler, D. W.; Houston, P. L. *J. Chem. Phys.* **1987**, 87, 1445.
- Eppink, A. T. J. B.; Parker, D. H. *Rev. Sci. Instrum.* **1997**, 68, 3477.
- Townsend, D.; Minitti, M. P.; Suits, A. G. *Rev. Sci. Instrum.* **2003**, 74, 2530.
- Li, W.; Chambreau, S. D.; Lahankar, S. A.; Suits, A. G. *Rev. Sci. Instrum.* **2005**, 76, 063106.
- Suits, A. G.; Bontuyan, L. S.; Houston, P. L.; Whitaker, B. J. *J. Chem. Phys.* **1992**, 96, 8618.
- Kitsopoulos, T. N.; Buntine, M. A.; Baldwin, D. P.; Zare, R. N.; Chandler, D. W. *Science* **1993**, 260, 1605.
- Liu, X.; Gross, R. L.; Hall, G. E.; Muckerman, J. T.; Suits, A. G. *J. Chem. Phys.* **2002**, 117, 7947.
- Li, W.; Lucchese, R. R.; Doyuran, A.; Wu, Z.; Loos, H.; Hall, G. E.; Suits, A. G. *E. Phys. Rev. Lett.*, in press.
- Bracker, A. S.; Wouters, E. R.; Suits, A. G.; Vasyutinskii, O. S. *J. Chem. Phys.* **1999**, 110, 6749.
- Liu, X.; Gross, R. L.; Suits, A. G. *Science* **2001**, 294, 2527.
- Suits, A.; Continetti, R. E. Imaging in chemical dynamics: The state of the art. In *Imaging in Chemical Dynamics*; Suits, A., Continetti, R. E., Eds.; American Chemical Society: Washington DC, 2000; p 1.
- Imaging in Molecular Dynamics*; Whitaker, B. J., Ed.; Cambridge University Press: Cambridge, U.K., 2003.
- Eppink, A. T. J. B.; W., S.-M.; Whitaker, B. J. Reconstruction Methods. In *Imaging in Molecular Dynamics*; Whitaker, B. J., Ed.; Cambridge University Press: Cambridge, U.K., 2003; p 65.
- Suits, A. G.; Miller, R. L.; Bontuyan, L. S.; Houston, P. L. *J. Chem. Soc., Faraday Trans.* **1993**, 89, 1443.
- Mo, Y.; Katayanagi, H.; Suzuki, T. *J. Chem. Phys.* **1999**, 110, 2029.
- Nestorov, V. K.; Hinchliffe, R. D.; Uebera, R.; Cline, J. I.; Lorentz, K. T.; Chandler, D. W. *J. Chem. Phys.* **2001**, 115, 7881.
- Bracker, A. S.; Wouters, E. R.; Suits, A. G.; Lee, Y. T.; Vasyutinskii, O. S. *Phys. Rev. Lett.* **1998**, 80, 1626.
- Bass, M. J.; Brouard, M.; Clark, A. P.; Vallance, C. *J. Chem. Phys.* **2002**, 117, 8723.
- Bass, M. J.; Brouard, M.; Clark, A. P.; Vallance, C.; Martinez-Haya, B. *Phys. Chem. Chem. Phys.* **2003**, 5, 856.
- Brouard, M.; Clark, A. P.; Vasyutinskii, O. S.; Vallance, C. *J. Chem. Phys.* **2003**, 119, 771.
- Brouard, M.; Cireasa, R.; Clark, A. P.; Preston, T. J.; Vallance, C.; Groenenboom, G. C.; Vasyutinskii, O. S. *J. Phys. Chem. A* **2004**, 108, 7965.
- Tonokura, K.; Suzuki, T. *Chem. Phys. Lett.* **1994**, 224, 1.
- Gebhardt, C. R.; Rakitzis, T. P.; Samartzis, P. C.; Ladopoulos, V.; Kitsopoulos, T. N. *Rev. Sci. Instrum.* **2001**, 72, 3848.
- Townsend, D.; Minitti, M. P.; Suits, A. G. *Rev. Sci. Instrum.* **2003**, 74, 2530.
- Lin, J. J.; Zhou, J.; Shiu, W.; Liu, K. *Rev. Sci. Instrum.* **2003**, 74, 2495.
- Ni, H.; Serafin, J. M.; Valentini, J. J. *J. Chem. Phys.* **2000**, 113, 3055.
- Picconatto, C. A.; Ni, H.; Srivastava, A.; Valentini, J. J. *J. Chem. Phys.* **2001**, 114, 7073.
- Vissers, G. W. M.; Oudejans, L.; Miller, R. E.; Groenenboom, G. C.; van der Avoird, A. *J. Chem. Phys.* **2004**, 120, 9487.
- Mordaunt, D. H.; Ashfold, M. N. R.; Dixon, R. N. *J. Chem. Phys.* **1994**, 100, 7360.
- Hsieh, C. H.; Lee, Y. S.; Fujii, A.; Lee, S. H.; Liu, K. *Chem. Phys. Lett.* **1997**, 277, 33.
- Lin, C.; Witinski, M. F.; Davis, H. F. *J. Chem. Phys.* **2003**, 119, 251.
- Ho, P.; Bamford, D. J.; Buss, R. J.; Lee, Y. T.; Moore, C. B. *J. Chem. Phys.* **1982**, 76, 3630.
- Moore, C. B.; Weisshaar, J. C. *Annu. Rev. Phys. Chem.* **1983**, 34, 525.
- Bamford, D. J.; Filseth, S. V.; Foltz, M. F.; Hepburn, J. W.; Moore, C. B. *J. Chem. Phys.* **1985**, 82, 3032.
- Buttenhoff, T. J.; Carleton, K. L.; Chuang, M. C.; Moore, C. B. *J. Chem. Soc., Faraday Trans.* **1989**, 85, 1155.
- van Zee, R. D.; Foltz, M. F.; Moore, C. B. *J. Chem. Phys.* **1993**, 99, 1664.
- Balko, B. A.; Zhang, J.; Lee, Y. T. *J. Chem. Phys.* **1992**, 97, 935.
- Butler, L. J.; Neumark, D. M. *J. Phys. Chem.* **1996**, 100, 12801.
- Steinfeld, J. I.; Francisco, J. S.; Hase, W. L. *Chemical Kinetics and Dynamics*; Prentice Hall: Upper Saddle River, NJ, 1998.
- Eyring, H. *J. Chem. Phys.* **1935**, 3, 107.
- Evans, M. G.; Polyani, M. *Trans. Faraday Soc.* **1935**, 31, 875.
- Marcus, R. A. *Laser Chem.* **1983**, 2, 203.
- Baer, T.; Hase, W. L. *Unimolecular Reaction Dynamics: Theory and Experiment*; Oxford University Press: Oxford, U.K., 1996.
- Moore, C. B. *Faraday Discuss.* **1995**, 102, 1.
- Schinke, R. *Photodissociation Dynamics*; Cambridge University Press: Cambridge, U.K., 1993.
- Debarre, D.; Lefebvre, M.; Pealat, M.; Taran, J. P. E.; Bamford, D. J.; Moore, C. B. *J. Chem. Phys.* **1985**, 83, 4476.
- Buttenhoff, T. J.; Carleton, K. L.; Moore, C. B. *J. Chem. Phys.* **1990**, 92, 377.
- Scuseria, G. E.; Schafer, H. F. *J. Chem. Phys.* **1989**, 90, 3629.
- Chang, Y.-T.; Minichino, C.; Miller, W. H. *J. Chem. Phys.* **1992**, 96, 4341.
- Chen, W.; Hase, W. L.; Schlegel, H. B. *Chem. Phys. Lett.* **1994**, 228, 436.
- Marcy, T. P.; Diaz, R. R.; Heard, D.; Leone, S. R.; Harding, L. B.; Klippenstein, S. J. *J. Phys. Chem. A* **2001**, 105, 8361.
- Knyazev, V. D. *J. Phys. Chem. A* **2002**, 106, 8741.
- Yan, T.; Doubleday, C.; Hase, W. L. *J. Phys. Chem. A* **2004**, 108, 9863.
- Sun, L.; Song, K.; Hase, W. L. *Science* **2002**, 296, 875.
- Mohammad, F.; Morris, V. R.; Fink, W. H.; Jackson, W. M. *J. Phys. Chem.* **1993**, 97, 11590.
- Townsend, D.; Lahankar, S. A.; Lee, S. K.; Chambreau, S. D.; Suits, A. G.; Zhang, X.; Rheinecker, J.; Harding, L. B.; Bowman, J. M. *Science* **2004**, 306, 1158.
- Zhang, X. B.; Rheinecker, J. L.; Bowman, J. M. *J. Chem. Phys.* **2005**, 122.
- Ahmed, M.; Peterka, D. S.; Regan, P.; Liu, X. H.; Suits, A. G. *Chem. Phys. Lett.* **2001**, 339, 203.
- Liu, X. H.; Gross, R. L.; Suits, A. G. *Science* **2001**, 294, 2527.
- Hatano, Y. Dynamics of Supereccited Molecules. In *Dynamics of Excited Molecules*; Kuchitsu, K., Ed.; Elsevier: Amsterdam 1994; p 151.
- Berkowitz, J. Photoion Pair Formation. In *VUV and Soft X-ray Photoionization*; Becker, U., Shirley, D. A., Eds.; Plenum: New York, 1996.

- (72) Suto, K.; Sato, Y.; Reed, C. L.; Skorokhodov, V.; Matsumi, Y.; Kawasaki, M. *J. Phys. Chem. A* **1997**, *101*, 1222.
- (73) Gross, R. L.; Liu, X.; Suits, A. G. *Chem. Phys. Lett.* **2003**, *376*, 710.
- (74) Gross, R. L.; Liu, X.; Suits, A. G. *Chem. Phys. Lett.* **2002**, *362*, 229.
- (75) Park, C. R.; Wiesenfeld, J. R. *J. Chem. Phys.* **1991**, *95*, 8166.
- (76) Yu, H. G.; Muckerman, J. T. *J. Phys. Chem. A* **2004**, *108*, 8615.
- (77) Mitchell, A. C. G. *Z. Phys.* **1928**, *49*, 228.
- (78) van Brunt, R. J.; Zare, R. N. *J. Chem. Phys.* **1968**, *48*, 4304.
- (79) Townsend, D.; Lee, S. K.; Suits, A. G. *Chem. Phys.* **2004**, *301*, 197.
- (80) Lee, S. K.; Townsend, D.; Vasyutinskii, O. S.; Suits, A. G. *Phys. Chem. Chem. Phys.* **2005**, *7*, 1650.
- (81) Siebbeles, L. D. A.; Glass-Maujean, M.; Vasyutinskii, O. S.; Beswick, J. A.; Roncero, O. *J. Chem. Phys.* **1994**, *100*, 3610.
- (82) Teule, T. M.; Groenenboom, G. C.; Neyer, D. W.; Chandler, D. W.; Janssen, M. H. M. *Chem. Phys. Lett.* **2000**, *320*, 177.
- (83) Dylewski, S. M.; Geiser, J. D.; Houston, P. L. *J. Chem. Phys.* **2001**, *115*, 7460.
- (84) Hancock, G.; Pearson, P. J.; Ritchie, G. A. D.; Tibbetts, D. F. *Phys. Chem. Chem. Phys.* **2003**, *5*, 5386.
- (85) Rakitzis, T. P.; Samartzis, P. C.; Kitsopoulos, T. N. *J. Chem. Phys.* **1999**, *111*, 10415.
- (86) Bracker, A. S.; Wouters, E. R.; Suits, A. G.; Vasyutinskii, O. S. *J. Chem. Phys.* **1999**, *110*, 6749.
- (87) Wouters, E. R.; Ahmed, M.; Peterka, D. S.; Bracker, A. S.; Suits, A. G.; Vasyutinskii, O. S. Imaging the atomic alignment and orientation in photodissociation. In *Imaging in Chemical Dynamics*; Suits, A. G., Ed.; American Chemical Society: Washington, DC, 2000; p 238.
- (88) Smolin, A. G.; Vasyutinskii, O. S.; Wouters, E. R.; Suits, A. G. *J. Chem. Phys.* **2004**, *121*, 6759.
- (89) Mo, Y.; Suzuki, T. *J. Chem. Phys.* **1998**, *109*, 4691.
- (90) Rakitzis, T. P.; Kandel, S. A.; Zare, R. N. *J. Chem. Phys.* **1998**, *108*, 8291.
- (91) Alexander, A. J.; Zare, R. N. *Acc. Chem. Res.* **2000**, *33*, 199.
- (92) Stolow, A.; Bragg, A. E.; Neumark, D. M. *Chem. Rev.* **2004**, *104*, 1719.
- (93) Davies, J. A.; Continetti, R. E.; Chandler, D. W.; Hayden, C. C. *Phys. Rev. Lett.* **2000**, *84*, 5983.
- (94) Vieuxmaire, O. P. J.; Nahler, N. H.; Jones, J. R.; Dixon, R. N.; Ashfold, M. N. R. *Mol. Phys.* **2005**, *103*, 1677.
- (95) Brixner, T.; Gerber, G. *ChemPhysChem* **2003**, *4*, 418.
- (96) Dantus, M.; Lozovoy, V. V. *Chem. Rev.* **2004**, *104*, 1813.
- (97) Schmittenmaer, C. A. *Chem. Rev.* **2004**, *104*, 1759.
- (98) Underwood, J. G.; Sussman, B. J.; Stolow, A. *Phys. Rev. Lett.* **2005**, *94*.
- (99) Yang, H.; Xie, X. S. *J. Chem. Phys.* **2002**, *117*, 10965.
- (100) Kapteyn, H. C.; Murnane, M. M.; Christov, I. R. *Phys. Today* **2005**, *58*, 39.
- (101) Gibson, E. A.; Zhang, X. S.; Popmintchev, T.; Paul, A.; Wagner, N.; Lytle, A.; Christov, I. P.; Murnane, M. M.; Kapteyn, H. C. *IEEE J. Select. Top. Quantum Electron.* **2004**, *10*, 1339.